

www.acsami.org Research Article

# Bioconjugation of Active Ingredients to Plant Viral Nanoparticles Is Enhanced by Preincubation with a Pluronic F127 Polymer Scaffold

Matthew D. Shin, Justin D. Hochberg, Jonathan K. Pokorski, and Nicole F. Steinmetz\*



Cite This: https://doi.org/10.1021/acsami.1c13183



**ACCESS** 

Metrics & More

Article Recommendations

SI Supporting Information

ABSTRACT: Proteinaceous nanoparticles can be used to deliver large payloads of active ingredients, which is advantageous in medicine and agriculture. However, the conjugation of hydrophobic ligands to hydrophilic nanocarriers such as plant viral nanoparticles (plant VNPs) can result in aggregation by reducing overall solubility. Given the benefits of hydrophilic nanocarrier platforms for targeted delivery and multivalent ligand display, coupled with the versatility of hydrophobic drugs, contrast agents, and peptides, this is an issue that must be addressed to realize their full potential. Here, we report two preincubation strategies that use a Pluronic F127 polymer scaffold to prevent the aggregation of conjugated plant VNPs: a plant VNP–polymer precoat (COAT) and an active ingredient formulation



combined with a plant VNP-polymer precoat (FORMCOAT). The broad applications of these modified conjugation strategies were highlighted by testing their compatibility with three types of bioconjugation chemistry: *N*-hydroxysuccinimide ester—amine coupling, maleimide—thiol coupling, and copper(I)-catalyzed azide—alkyne cycloaddition (click chemistry). The COAT and FORMCOAT strategies promoted efficient bioconjugation and prevented the aggregation that accompanies conventional bioconjugation methods, thus improving the stability, homogeneity, and translational potential of plant VNP conjugates in medicine and agriculture.

KEYWORDS: bioconjugation, plant virus nanoparticles, peptides and proteins, small-molecule drugs, agrochemicals, biopolymers, Pluronic F127

#### 1. INTRODUCTION

Bioconjugation involves the formation of covalent bonds between large biomolecules and smaller synthetic structures. One of the main applications of bioconjugation is the conversion of such biomolecules into nanocarriers that encapsulate or display active ingredients for medical or agricultural applications. Some nanocarriers are designed to encapsulate their cargo without bioconjugation, including liposomes with hydrophilic exterior and hydrophobic interior compartments. Others are based on biopolymers, protein nanoparticles,<sup>2</sup> or viruses, and bioconjugation covalently attaches the cargo to the external or internal surface. The cargo may comprise drugs, therapeutic peptides/proteins, peptide/protein antigens, cell/organelle-specific peptide ligands for cell targeting and trafficking, fluorophores, or contrast agents for tracking and imaging, as well as agrochemicals for pesticide delivery.3 Nanocarriers offer many advantages for cargo delivery including the enhanced solubility of hydrophobic ligands, controlled and sustained drug release, targeted delivery to specific tissues, and multivalent ligand display, which allows the number, spacing, and avidity of ligands to be optimized.4

Plant virus nanoparticles (plant VNPs) are among the most versatile nanocarrier platforms. They are biocompatible and biodegradable but are noninfectious in mammals and thus offer a higher degree of safety than the animal viruses used as genedelivery vectors. They have also evolved as mobile nanocarriers to navigate plants and soil and can therefore be repurposed for precision farming. Plant VNPs come in a variety of shapes and sizes, including icosahedral forms and high-aspect-ratio nanorods or filaments with sizes in the range of 30-500 nm. Many plant VNPs are self-assembled supramolecular complexes based on simple coat protein (CP) units featuring solventaccessible interior and exterior surfaces whose various amino acids provide 'chemical handles' for bioconjugation. We have previously used tobacco mosaic virus (TMV-Lys, with a Lys substitution at amino acid position 158),6 tobacco mild green mosaic virus (TMGMV),7 and cowpea mosaic virus

Received: July 13, 2021 Accepted: November 26, 2021



Table 1. Summary of Ligand Properties<sup>a,b</sup>

ligand type	peptide/small molecule*	MW (Da)	Log P <sup>a</sup>	isoelectric point (pH) <sup>b</sup>	net charge @ pH 7 <sup>b</sup>	estimated water solubility <sup>b</sup>	observed water solubility
peptide epitope for vaccine	CH401-rat	2922	1.19	8.54	0.9	poor	poor
	myostatin 1	2092	1.06	8.96	1.2	poor	good
	COVID-106	2043	0.84	9.12	0.9	poor	poor
	COVID-153	2158	0.98	9.73	2	poor	poor
	COVID-454	2164	0.32	8.79	0.9	poor	poor
	COVID-826	2380	0.27	10.08	1.9	good	good
targeting peptide	F3	3707	0.81	11.08	7.9	good	good
	ScG3	1809	0.27	8.96	1	poor	good
therapeutic peptide	ApoAI-4FN	2631	1.53	6.36	-0.1	good	good
agrochemical	avermcetin-azide*	950	4.22				
fluorophore	Cy5.5 NHS ester*	768	3.08				
ligand type	peptide/small molecule*		S				
peptide epitope for vaccine	CH401-rat	YQDMVLWI	(DVFRKNN				
	myostatin 1	CGGGVFLQ	KYPHTHLV				
	COVID-106	<u>CGGG</u> FASTI	EKSNIIRGV				
	COVID-153	CGGGPFLG	VYYHKNNK				
	COVID-454	CGGGNNLD	SKVGGNYN				
	COVID-826	CGGGPSKPS	SKRSFIEDL				
targeting peptide	F3	KDEPQRRSA	ARLSAKPAF				
	ScG3	<u>CSGGG</u> WGV	VSLSHGYQ				
therapeutic peptide	ApoAI-4FN	CSGGG DWF	KAFYDKVA				
agrochemical	avermectin-azide*			=			
fluorophore	Cy5.5 NHS ester*			-	_		

<sup>&</sup>quot;Calculated using ALOGPS2.1 (log *P* is the octanol/water partition coefficient, with higher values representing increasing lipophilicity).

\*\*Calculated using PepCalc (the isoelectric point is the pH condition at which the net charge of the peptide is zero).

(CPMV)<sup>8,9</sup> for various applications targeting human and plant health. Each plant VNP has been extensively characterized and the surface chemistry is understood,<sup>7,10,11</sup> allowing functionalization for diverse applications.<sup>12–14</sup> Furthermore, multifunctional conjugation can be achieved by the multiplexed targeting of lysine, cysteine, glutamate/aspartate, and/or tyrosine side chains.<sup>15</sup>

Although plant VNP scaffolds offer a high degree of tunability, the conjugation of hydrophobic cargo molecules can reduce overall solubility, affecting structural integrity and yields. We therefore evaluated the use of Pluronic F127 (F127), a nonionic triblock-copolymer comprising a core block of hydrophobic poly(propylene oxide) capped by a terminal block of repeating poly(ethylene oxide) at each end of the molecule. This surfactant is approved as a pharmaceutical excipient and has been used as a wetting/solubilizing agent in the manufacture of micro/nanoparticles and the micellization of hydrophobic drugs or peptides. <sup>16–23</sup> It has also been used as a coating to protect TMV and ferritin. <sup>24</sup> However, to the best of our knowledge, it has not been used thus far to facilitate the bioconjugation of plant VNPs to hydrophobic ligands.

F127 does not covalently modify nanoparticles or their payloads, but chemically modified derivatives of F127 have been fused to ligands and drugs either by coating nanoparticles composed of PLGA, SPION, or chitosan or precipitation within them.<sup>25–27</sup> We exploited the intrinsic ability of unmodified F127 to coat plant VNPs and solubilize hydrophobic ligands to determine whether a preincubation step can facilitate bioconjugation yielding stable and soluble conjugates. We compared plant VNP–polymer precoat (COAT) and

ligand formulation plus plant VNP—polymer precoat (FORM-COAT) strategies using a ligand library featuring near-infrared dyes for biomedical imaging, pesticides for precision farming, therapeutic proteins for drug delivery, disease-targeting peptides, and peptide antigen vaccine candidates (Table 1). We tested N-hydroxysuccinimide (NHS) ester—amine coupling, copper(I)-catalyzed azide—alkyne cycloaddition (click chemistry), and maleimide—thiol coupling in the presence and absence of F127 and then characterized the products by digital imaging, sodium dodecylsulfate polyacrylamide gel electrophoresis (SDS-PAGE), dynamic light scattering (DLS), transmission electron microscopy (TEM), and ultraviolet—visible (UV—vis) spectroscopy. We focused on plant VNP—ligand conjugates that undergo visible aggregation when prepared using conventional protocols.

# 2. RESULTS AND DISCUSSION

**2.1. Selection of Ligands.** We selected 11 candidates from a library of ligands that have previously shown a tendency to trigger the aggregation of conjugated plant VNPs (Table 1). We included cyanine5.5 (Cy5.5) because it is widely used for biomedical imaging. The sulfonated version ( $\log P = 1.91$ ) is highly soluble in water and allows stable conjugation, whereas the nonsulfonated version ( $\log P = 4.94$ ) has proven more challenging in our hands. We obtained the NHS ester of nonsulfonated Cy5.5 for conjugation to solvent-exposed lysine side chains on CPMV and TMV.

We included avermectin as a model hydrophobic small-molecule drug/pesticide (log P=4.37) representing other hydrophobic insecticides such as moxidectin (log P=5.30)

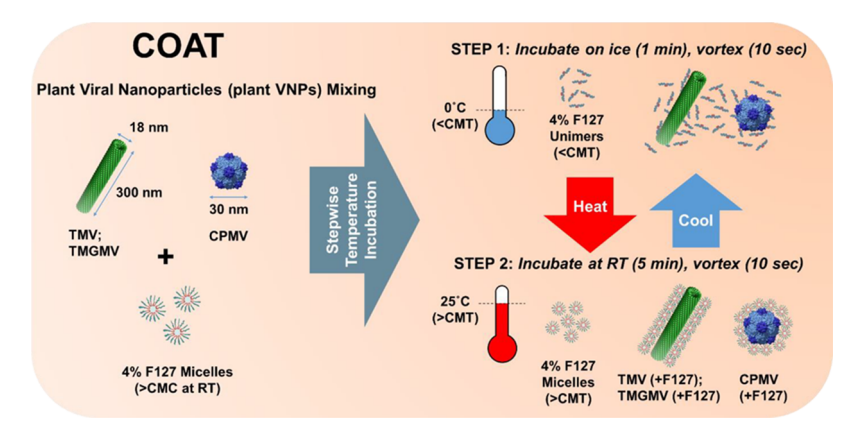
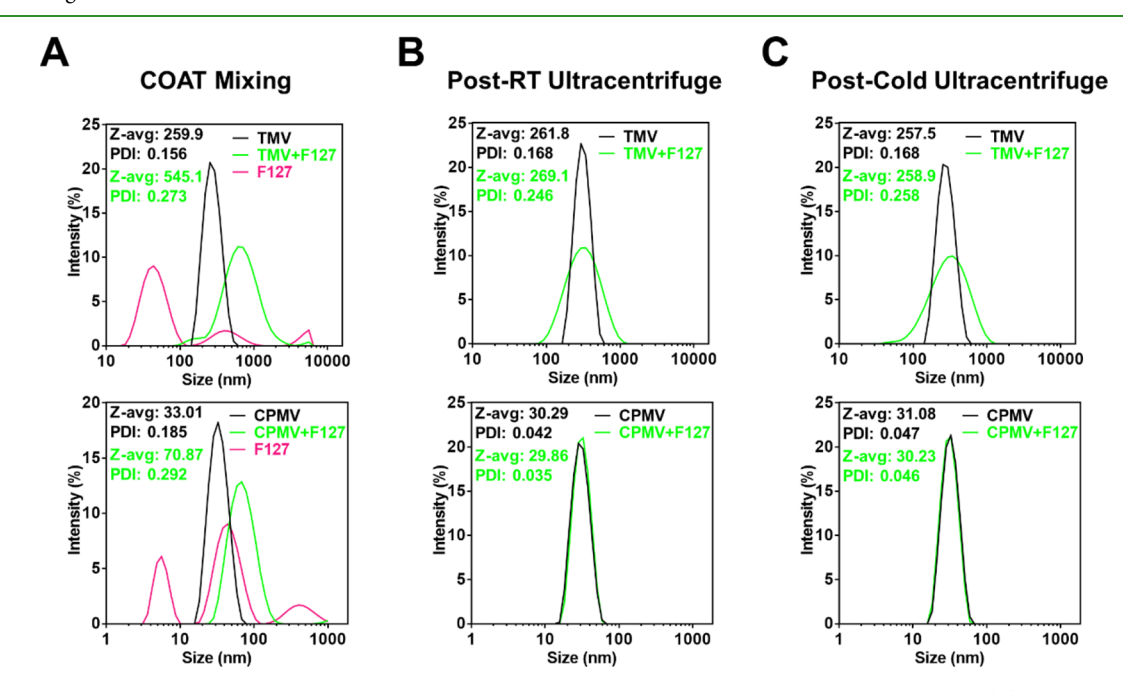


Figure 1. COAT strategy. Plant VNPs are mixed with 4% (w/w) F127 and then processed by varying the temperature. The samples are first incubated on ice to promote the formation of F127 unimers before shifting to room temperature to promote F127 micellization and subsequent plant VNP coating.



**Figure 2.** DLS data showing plant VNP size following the COAT process and fixed-temperature ultracentrifugation. (A) Plant VNPs mixed with F127 using the COAT strategy at 19.5 °C. (B) Coated plant VNPs are purified by ultracentrifugation at 25 °C. (C) Coated plant VNPs are purified by ultracentrifugation at 4 °C. Top row = TMV and bottom row = CPMV.

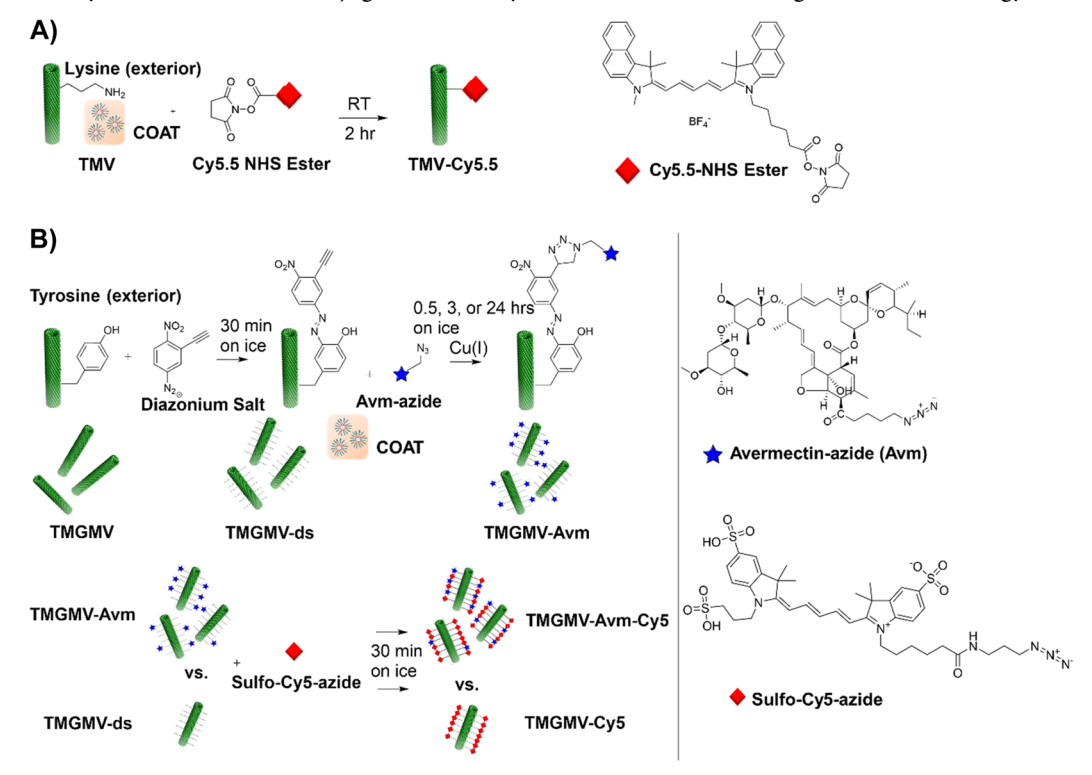
and afidopyropen (log P=3.08) as well as drugs such as doxorubicin (log P=1.41) and paclitaxel (log P=3.20). Nanocarrier conjugates are promising formulations to stabilize avermectin and enhance its soil mobility.<sup>7,30</sup> Avermectin azide (Avm) was synthesized in-house (Figure S1) and was characterized by electrospray ionization mass spectrometry (ESI-MS) (Figure S2).

Finally, we included nine peptides with medical applications. CH401R is an epitope of human epidermal growth factor receptor 2 (HER2) and a candidate cancer vaccine. We previously demonstrated the ability of CPMV-CH401R conjugates to delay tumor progression in mouse models of HER2<sup>+</sup> breast cancer.<sup>31</sup> Myo1 is a peptide epitope of myostatin, which has been proposed as a muscle growth vaccine.<sup>32,33</sup> Four peptide epitopes derived from the SARS-CoV-2 S-protein were selected as candidates for a COVID-19 vaccine.<sup>34–38</sup> F3 and ScG3 were selected as model cell-targeting peptides. F3 targets the cell shuttle molecule nucleolin, and we have previously shown that drug-loaded

plant VNPs displaying this peptide are more efficient at killing cancer cells.<sup>39</sup> ScG3 targets an inflammatory regulator (S100 calcium-binding protein A9), and we have previously used plant VNPs displaying this peptide for the imaging of atherosclerotic plaques.<sup>39,40</sup> Finally, 4FN is a therapeutic peptide derived from apolipoprotein A1 that promotes cholesterol efflux from foam cells and also suppresses tumor activity. 41 All nine peptides were synthesized with a GGGSC or GGGC extension to enable conjugation via the heterobifunctional maleimide linker SM(PEG)4. This simultaneously reacts with terminal cysteine residues on the peptides and a succinimidyl group that binds solvent-exposed lysine residues on CPMV and TMV. The molecular weight of the peptides ranged from 1741 to 3707 Da, with log P values of -0.89 to 1.53 (determined using ALogPS), isoelectric points of 6.21 to 11.08 (determined using PepCalc), and a net charge at pH 7 of −0.1 to 7.9 (also determined using PepCalc).

**2.2.** Coating Plant VNPs with F127 (COAT Strategy). *2.2.1.* General Strategy. The plant VNPs were coated with

Scheme 1. Summary of Plant VNP Bioconjugation with Cy5.5 and Avermectin Using the COAT Strategy<sup>a</sup>



<sup>a</sup>(A) Synthesis of Cy5.5-conjugated TMV via NHS ester coupling and (B) synthesis of avermectin-conjugated TMGMV via Cu-catalyzed click chemistry.

F127 as a temporary scaffold in a procedure described as the COAT strategy (Figure 1). F127 has a critical micelle concentration of 0.725% (w/w) at 25 °C, and we used a 4% (w/w) solution for coating, which thus favors the formation of micelles. The plant VNP and F127 solutions were combined, and the sample temperature was reduced to below the critical micelle temperature (CMT) of 19.5–21.5 °C to promote the homogeneous distribution of F127 unimers. Then the temperature was raised to promote micellization and plant VNP coating. This process is also reversible (lowering the temperature again can promote "decoating" and plant VNP purification).

The COAT strategy was applied successfully to CPMV and TMV as confirmed by DLS (Figure 2). The DLS intensity plots of plant VNP(+F127) particles showed an increase in diameter, which indicated successful coating with F127 micelles. The Z-average of TMV increased from 259.9 nm (untreated) to 545.1 nm (after the COAT process) and the polydispersity index (PDI) increased from 0.165 to 0.273. Similarly, the Z-average of CPMV increased from 33.01 nm (untreated) to 70.87 nm (after the COAT process), and the PDI increased from 0.185 to 0.292. The plant VNP peaks after the COAT process were larger than the starting peaks of either plant VNP or F127. In the mixed sample, the disappearance of the characteristic F127 unimer, micellar, and supramolecular micellar peaks probably reflects favorable coating interactions on the plant VNP surface.

The DLS spectra of CPMV and TMV following ultracentrifugation at 4 °C or room temperature indicated that the F127 coating can be removed, although there was evidence of residual F127 still adsorbed to TMV after purification. (Figure 2B,C). In contrast, no clear indications of residual F127 were present for purified CPMV (Figure 2B,C). For CPMV, the Zaverage and PDI after ultracentrifugation at 4 °C indicated the recovery of pure CPMV with a diameter of ~30 nm and a narrow PDI ( $\sim$ 0.04). For TMV, the Z-average after ultracentrifugation at 4 °C matched that of untreated TMV (~260 nm), but the PDI was still higher (0.26) than that of untreated TMV (0.17), which may indicate a population of TMV with a residual surface polymer (Figure 2C). Because room temperature is well above the CMT of 4% (w/w) F127, we hypothesized that purification at room temperature would yield coated plant VNPs. This was not the case for CPMV, as no significant difference in Z-average or PDI was observed between purified CPMV and uncoated CPMV control (both  $\sim$ 30 nm and PDI < 0.05). (Figure 2B). However, Z-average of the TMV particles was 269 nm (compared to 262 nm for untreated particles), and the PDI was 0.24 (compared with 0.17 for untreated particles), again suggesting the presence of a residual surface polymer. We also detected residual F127 on TMV particles by Fourier transform infrared (FT-IR) spectroscopy (Figure S3) and observed a weaker enzymelinked immunosorbent assay (ELISA) signal when coated particles were probed with polyclonal antibodies against TMV (Figure S4). These data suggest that cold-temperature ultracentrifugation is an effective method to remove F127 from CPMV particles but is not as effective for TMV.

The size, charge, and multivalent display density of conjugated ligands can all play a role in the steric and electrostatic surface environment of plant VNPs and thus influence the F127 coating process. Indeed, we observed more efficient F127 removal from chemically conjugated TMV compared to native TMV and its conjugates (Figure S5). Interactions between the terminal poly(ethylene oxide) groups

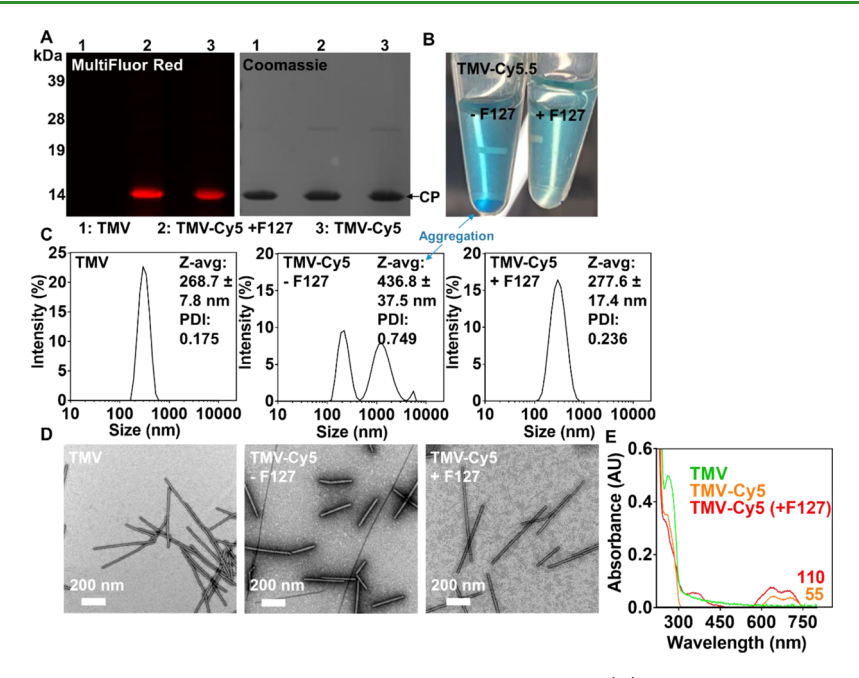


Figure 3. Chemical conjugation of Cy5.5 dye to TMV using amine-reactive NHS chemistry. (A) SDS-PAGE analysis of TMV-Cy5.5 particles using MultiFluor Red (632 nm) and Coomassie Brilliant Blue and the Fluorchem M System. CP = TMV coat protein ( $\sim$ 17 kDa). (B) Photograph of TMV-Cy5.5 particles with/without (+/-) the COAT preincubation strategy, showing aggregation in the sample without preincubation. (C) Corresponding DLS intensities of TMV particles ( $Z_{av}$  data are mean values  $\pm$  SD, n = 3). (D) Corresponding TEM images of negatively stained TMV particles. (E) UV/vis absorbance of native TMV and Cy5-conjugated to TMV(+/-F127) after a 30 min reaction.

of F127 micelles and the CP surface are thought to control F127 coating by physisorption, and the multivalent display of ligands on TMV may perturb these interactions thus reducing the 'holding power' of F127, resulting in narrower peak widths for TMV conjugates compared to native TMV. It has been reported that  $\alpha$ -cyclodextrin forms strong interactions with poly(ethylene oxide) units of F127 in solution and prohibits adsorption of F127 on the TMV surface. Therefore, further optimized purification methods for F127 removal from TMV could be developed which incorporate an  $\alpha$ -cyclodextrin incubation step to samples just prior to ultracentrifugation purification. Increasing the number of centrifugation purification steps may also improve F127 removal.

2.2.2. Small-Molecule Bioconjugation to Plant VNPs Using the COAT Strategy. For the conjugation of Cy5.5 to TMV (Scheme 1A), TMV samples coated with F127 at 28 molar equivalents per CP (and uncoated controls) were incubated with the hydrophobic Cy5.5-NHS ligand at two molar equivalents per CP. TMV-Cy5.5 conjugates were purified by low-temperature ultracentrifugation to remove excess dye and F127 and were then characterized by SDS-PAGE, DLS, and TEM (Figure 3). Conjugation of Cy5.5 to both coated and untreated particles was confirmed by SDS-PAGE, as evidenced by the colocalization of the Cy5.5 signal and TMV CP band (Figure 3A). However, the uncoated Cy5.5-conjugated particles were prone to aggregation, revealed by the cloudy solution (data not shown) and high sedimentation velocity, resulting in an observable pellet (Figure 3B). In contrast, the samples prepared using the COAT method were dispersed and soluble, with no visible signs of aggregation (Figure 3B). DLS data were consistent with these observations. The Z-average of the TMV-Cy5.5-(+F127) particles was 277.6 nm (PDI = 0.236) which is similar to that of the unconjugated TMV particles ( $Z_{av} = 268.7$  nm and PDI = 0.175) (Figure 2A). However, the Z-average of the

TMV-Cy5.5(-F127) particles was 436.8 nm (PDI = 0.749), resulting in a nonuniform, multimodal intensity profile indicating several different populations of particle sizes (Figure 3C). TEM imaging confirmed that the COAT method yielded structurally sound TMV-Cy5.5 nanoparticles (Figure 3D). TMV-Cy5.5(-F127) aggregates were not observed by TEM, but this probably reflects the removal of aggregates during the washing step. Two major populations were formed by the uncoated particles, one of which was more heavily aggregated than the other (as evident from the two DLS populations). Finally, we also evaluated the conjugation efficiency and found that the COAT method doubled the dye conjugation efficiency, resulting in 110 dye molecules conjugated per TMV-Cy5.5(+F127) particle compared to 55 dye molecules per TMV-Cy5.5(-F127) particle (Figure 3E). This difference was significant (p < 0.001; unpaired two-tailed Student's t-test; Figure S6).

For the conjugation of Avm to TMGMV (Scheme 1B), alkyne handles were introduced by reacting external tyrosine side chains with diazonium salt (3-ethynyl aniline, 15 molar equivalents per CP) to form a TMGMV-ds intermediate. This was purified by ultracentrifugation to remove excess diazonium salt and resuspended in 0.01 M potassium phosphate buffer (pH 7.4). The COAT procedure was then applied prior to Avm conjugation. TMGMV-ds samples were incubated with the hydrophobic Avm ligand (five molar equivalents per CP) for 30 min (+F127 particles) or for 3 or 24 h (-F127 particles), and conjugation was carried out using a Cu(I)-catalyzed azide-alkyne cycloaddition (click chemistry) protocol to form the TMGMV-Avm product.

TMGMV-Avm particles were purified by low-temperature ultracentrifugation to remove F127 and excess reagents. The resuspended TMGMV-Avm particles were vortexed, and an image was captured using a smartphone camera. The TMGMV-Avm(-F127) particles showed clear evidence of

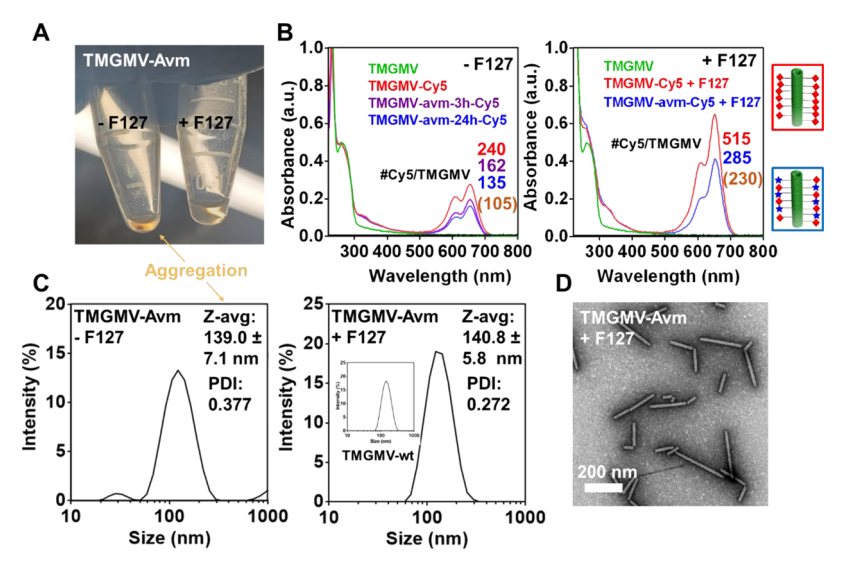
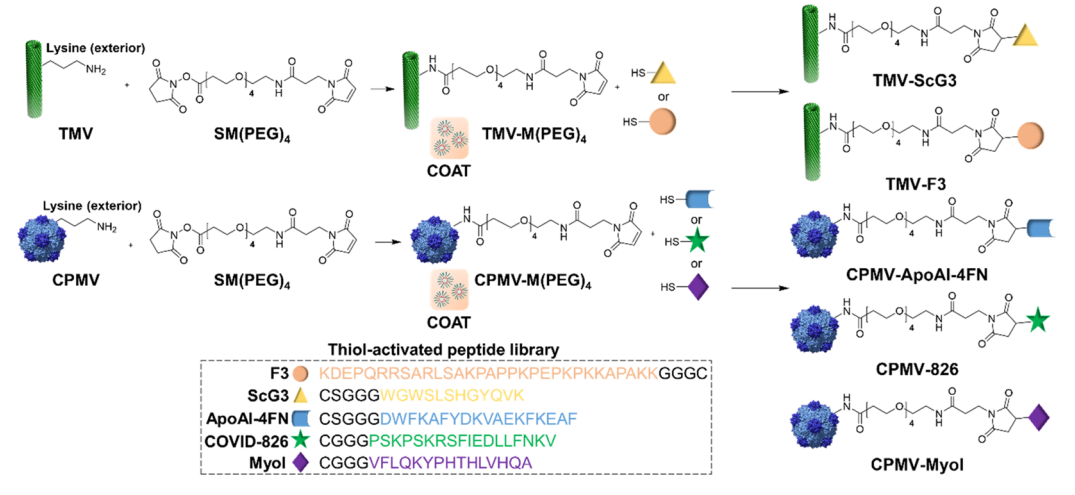


Figure 4. Chemical conjugation of Avm to TMGMV using Cu-catalyzed click chemistry. (A) Photograph of TMGMV-Avm particles with/without (+/-) the COAT preincubation strategy, showing aggregation in the sample without preincubation. (B) UV/vis absorbance of native TMGMV, Cy5-conjugated TMGMV, and Cy5-conjugated TMGMV-Avm(+/-F127). The left panel shows groups of TMGMV-Avm conjugates after 3 or 24 h, and the right panel shows a group of TMGMV-Avm conjugates after 30 min. The number in parentheses is the number of Avm ligands per TMGMV. (C) Corresponding DLS intensities of TMGMV particles ( $Z_{av}$  data are mean values  $\pm$  SD, n = 3). (D) Corresponding TEM images of negatively stained TMGMV particles.

Scheme 2. Synthesis of Peptide-Conjugated TMV and CPMV Particles Using a Dual-Functional M(PEG)<sub>4</sub> Linker with Maleimide-Thiol and NHS-Amine Chemistry<sup>a</sup>



<sup>a</sup>The COAT strategy was applied to the intermediate plant VNP-SM(PEG)₄ before peptide bioconjugation.

aggregation, resulting in a high sedimentation velocity and an observable pellet (Figure 4A). In contrast, the TMGMV-Avm(+F127) particles were dispersed and soluble, with no visible signs of aggregation (Figure 4A). The Z-average of the TMGMV-Avm particles was  $\sim$ 140 nm for both preparations, but the uncoated samples showed a higher degree of polydispersity (PDI = 0.272) compared to the coated particles (PDI = 0.084) (Figure 4C). TEM imaging confirmed that the COAT method yielded structurally sound TMGMV-Avm particles (Figure 4D). The images also revealed the presence of smaller or broken TMGMV nanoparticles, but this is a common phenomenon for rod-shaped plant viruses and is probably a TEM preparation artifact.

To determine the efficiency of conjugation, we used an indirect fluorescence assay in which TMGMV-ds and TMGMV-Avm particles were reacted for 30 min with sulfo-

Cy5.5-azide, and the difference in signal intensity was used to calculate the proportion of unused conjugation handles (Scheme 1B). This revealed that the COAT strategy doubled the conjugation efficiency, resulting in 230 Avm ligands per TMGMV-Avm(+F127) particle compared to 105 ligands per TMGMV-Avm(-F127) particle (Figure 4B). The coated particles were also more stable. Interestingly, in the same 30 min reaction window, the number of conjugated Cy5 dye molecules was 285 per TMGMV-Avm(+F127) particle but only 135-162 per TMGMV-Avm(-F127) particle (Figure 4B). This would suggest a lower efficiency of Avm conjugation, but we also observed an increase in Cy5 conjugation for the control TMGMV-ds(+F127) particles (515 dye molecules) compared to the TMGMV-ds(-F127) particles (240 dye molecules). These observations may reflect the presence of a residual F127 coating on the surface of TMGMV-ds control and TMGMV-Avm particles even after ultracentrifugation, and this may enhance the bioconjugation of Cy5 as observed for the corresponding TMV-Cy5 particles (Figure 3).

2.2.3. Peptide Bioconjugation to Plant VNPs Using the COAT Strategy. For the conjugation of targeting ligands F3 and ScG3 to TMV, and the therapeutic peptide ApoAI-4FN to CPMV (Scheme 2), lysine residues on each plant VNP were reacted with the SM(PEG)<sub>4</sub> linker (five molar equivalents per TMV CP or 3000 molar equivalents per CPMV particle) to form a maleimide intermediate, plant VNP-M(PEG)<sub>4</sub>. The COAT procedure was applied before the reaction of TMV with ScG3 or F3 (0.5 molar equivalents per CP) or the reaction of CPMV with ApoAI-4FN (200 molar equivalents per particle). In each case, uncoated particles were conjugated to the same peptides as controls. All samples were purified by low-temperature ultracentrifugation and washing followed by characterization using the methods described above (Figures 567).

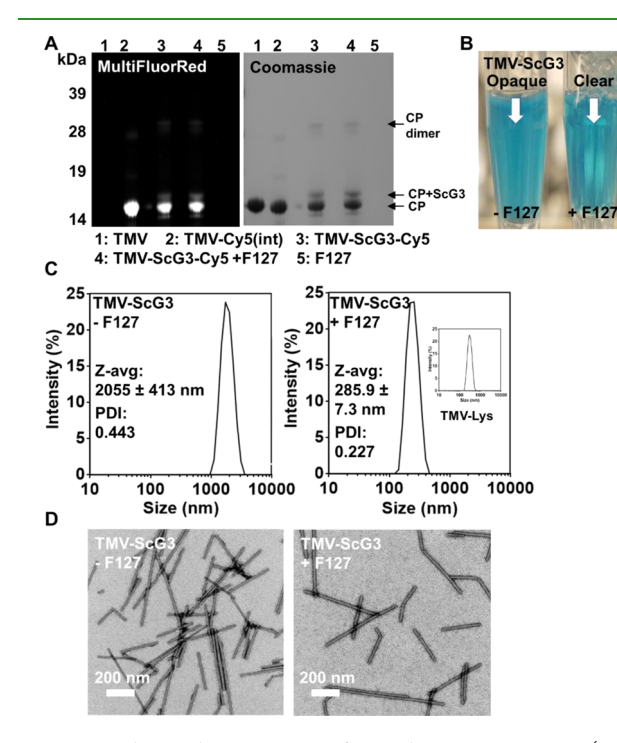
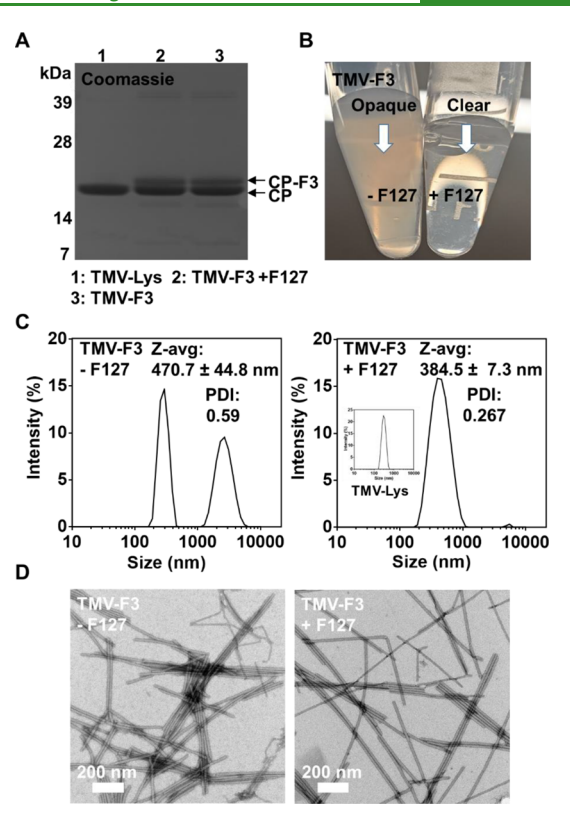


Figure 5. Chemical conjugation of peptide ScG3 via an SM(PEG)<sub>4</sub> linker to TMV, which is also labeled internally with Cy5. (A) SDS-PAGE analysis of TMV-ScG3 particles. CP = TMV coat protein ( $\sim$ 17 kDa). (B) Photograph of TMV-ScG3 particles with/without (+/-) the COAT preincubation strategy, showing aggregation in the sample without preincubation. (C) Corresponding DLS intensities of TMV particles ( $Z_{av}$  data are mean values  $\pm$  SD, n = 3). (D) Corresponding TEM images of negatively stained TMV particles.

The conjugation of TMV to ScG3 (~1.8 kDa) and F3 (~3.7 kDa) was confirmed by SDS-PAGE, which revealed the presence of higher-molecular-weight bands at ~19.3 kDa for CP-ScG3 (Figure 5A) and 21.2 kDa for CP-F3 (Figure 6A), in addition to the native TMV CP band at ~17.5 kDa (Figures 5A and 6A). Densitometric analysis indicated ~25% total CP modification regardless of whether or not the COAT method was used. Therefore, coating with F127 appeared to enhance the conjugation of small-molecule ligands but not peptides. However, the COAT strategy was shown to enhance the stability of plant VNP-peptide conjugates, as shown by the



**Figure 6.** Chemical conjugation of peptide F3 via an SM(PEG)<sub>4</sub> linker to TMV. (A) SDS-PAGE analysis of TMV-F3 particles. CP = TMV coat protein (~17 kDa). (B) Photograph of TMV-F3 particles with/without (+/—) the COAT preincubation strategy, showing aggregation in the sample without preincubation. (C) Corresponding DLS intensities of TMV particles ( $Z_{\rm av}$  data are mean values  $\pm$  SD, n = 3). (D) Corresponding TEM images of negatively stained TMV particles.

aggregation of the TMV-ScG3 and TMV-F3 samples prepared without F127 but not those prepared with F127 (Figures 5B and 6B). DLS confirmed heavy aggregation of the TMV-ScG3(-F127) particles ( $Z_{\rm av}$  > 2000 nm and PDI > 0.4) and the TMV-F3(-F127) particles ( $Z_{\rm av}$  ~ 470.7 nm and PDI = 0.59). In contrast, there was no evidence of aggregation for the TMV-ScG3(+F127) particles ( $Z_{\rm av}$  ~ 285.9 nm and PDI = 0.227) (Figures 5C and 6C), and although DLS revealed an increase in the hydrodynamic diameter of the TMV-F3(+F127) particles ( $Z_{\rm av}$  ~ 384.5 nm, PDI = 0.267), there was no sign of aggregation in the TMV-ScG3(+F127) or TMV-F3(+F127) TEM images (Figures 5D and 6D).

The conjugation of CPMV to ApoAI-4FN (~2.6 kDa) was also confirmed by SDS-PAGE, which revealed the presence of native CPMV small (S) and large (L) CP subunits, as well as higher-molecular-weight bands at ~26.6 kDa (S-CP-4FN) and ~44.6 kDa (L-CP-4FN) (Figure 7A). The COAT strategy promoted a small increase in conjugation efficiency (~59% vs ~57% for the S-CP and ~50% vs ~43% for the L-CP). The COAT strategy also increased the number of ApoAI-4FN peptides per CPMV from 61 to 66. As observed for the other conjugates, the CPMV-4FN(-F127) particles showed clear visual signs of aggregation, whereas the CPMV-4FN(+F127) particles showed good dispersion properties (Figure 7B). This was supported by the DLS data, which revealed a multimodal intensity profile for the CPMV-4FN(-F127) particles, indicating distinct populations with a Z-average of ~62.0 nm

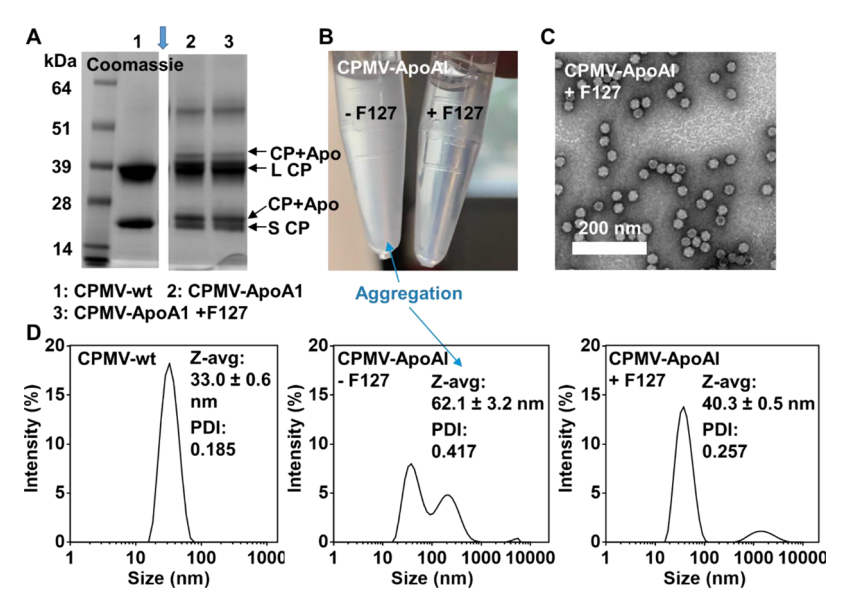


Figure 7. Chemical conjugation of peptide ApoAI via an SM(PEG)<sub>4</sub> linker to CPMV. (A) SDS-PAGE analysis of CPMV-ApoAI particles. S-CP = CPMV small coat protein ( $\sim$ 24 kDa) and L-CP = CPMV large coat protein ( $\sim$ 42 kDa). (B) Photograph of CPMV-ApoAI particles with/without (+/-) the COAT preincubation strategy, showing aggregation in the sample without preincubation. (C) Corresponding TEM images of negatively stained CPMV particles. (D) Corresponding DLS intensities of TMV particles ( $Z_{av}$  data are mean values  $\pm$  SD, n = 3).

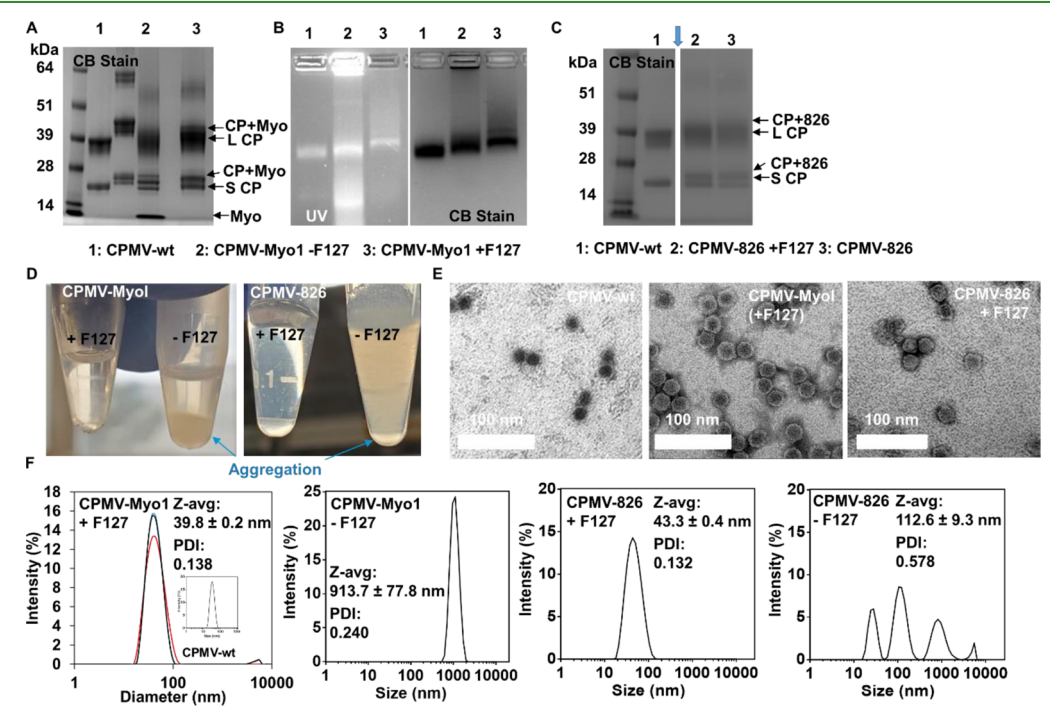


Figure 8. Chemical conjugation of peptides Myo1 and COVID-826 via maleimide-thiol conjugation to CPMV. (A) SDS-PAGE analysis of CPMV-Myo1 particles. S-CP = CPMV small coat protein ( $\sim$ 24 kDa) and L-CP = CPMV large coat protein ( $\sim$ 42 kDa). (B) Agarose gel electrophoresis of CPMV-Myo1 particles with/without (+/-) the COAT preincubation strategy. (C) SDS-PAGE analysis of CPMV-826 particles. (D) Photograph of CPMV-MyoI and CPMV-826 particles with/without (+/-) the COAT preincubation strategy, showing aggregation in the samples without preincubation. (E) Corresponding TEM images of negatively stained CPMV particles. (F) Corresponding DLS intensities of CPMV-Myo1 and CPMV-826 particles ( $Z_{av}$  data are mean values  $\pm$  SD, n = 3).

(PDI = 0.417). In contrast, the CPMV-4FN(+F127) particles were characterized by a Z-average of  $\sim$ 40.3 nm (PDI = 0.257), although we detected a low-intensity peak of larger particles contributing to the increase in size, which may indicate the presence of a small fraction of aggregated particles (Figure 7D). As for the other plant VNP conjugates described above, no aggregates were observed in the TEM images (Figure 7C).

Having established that the COAT method enhances the stability of TMV and CPMV when conjugated to hydrophobic peptides, we investigated whether this approach was compatible with the conjugation of peptide epitopes used to develop plant VNP-based vaccines. For the conjugation of peptide epitopes (MyoI and COVID-826) to CPMV (Scheme 2), lysine residues in the CP were reacted with the SM(PEG)<sub>4</sub>

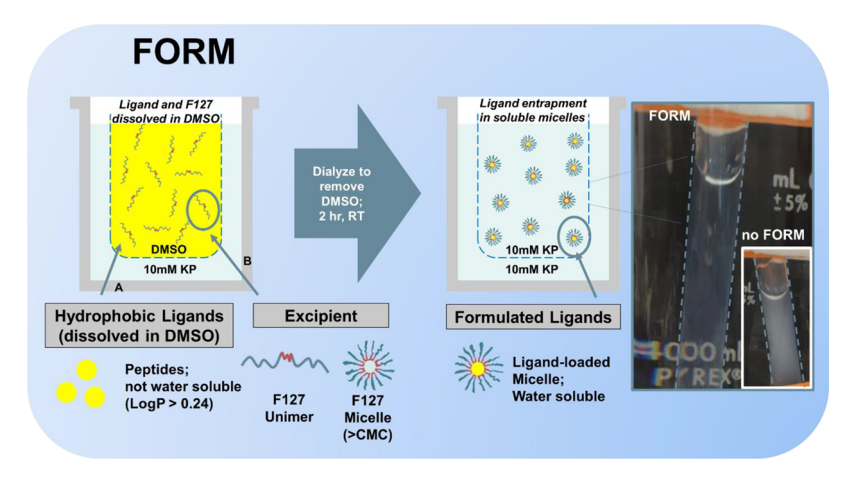
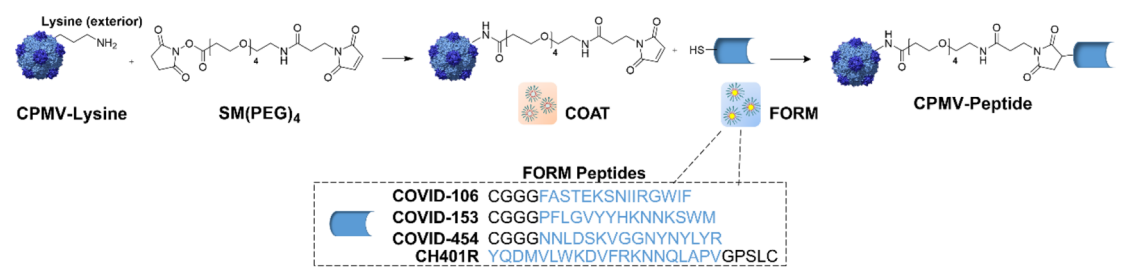


Figure 9. Formulation of hydrophobic peptides. Each peptide was first dissolved in DMSO to a concentration of 10 mg/mL before mixing with 10% (w/w) F127. The mixture was then transferred to dialysis tubing that allows solvent exchange while retaining the peptide. As DMSO leaves the dialysis bag, the F127 forms micelles and traps the hydrophobic peptides within the micelle corona. The now micellized, water-soluble peptide (formulated or FORM peptide) is collected for reaction with COATed plant VNPs in the FORMCOAT procedure.

Scheme 3. Conjugation of Peptides to CPMV via an SM(PEG)<sub>4</sub> Linker Using the FORMCOAT Strategy



"Formulated peptides are combined with plant VNP-M(PEG)<sub>4</sub> that has already been coated with F127. This maintains the hydrophobic peptides in a soluble form and facilitates conjugation.

I

linker (3000 molar equivalents per CPMV particle) to form the maleimide intermediate CPMV-M(PEG)<sub>4</sub>. The COAT procedure was applied before the reaction of CPMV with MyoI or COVID-826 (3000 molar equivalents per particle). In each case, uncoated particles were conjugated to the same peptides as controls. Samples were purified by low-temperature ultracentrifugation and washing followed by characterization using the methods described above.

The conjugation of CPMV to MyoI (~2.1 kDa) was confirmed by SDS-PAGE, which revealed the presence of native S-CP (~24 kDa) and L-CP (~42 kDa) subunits as well as higher-molecular-weight bands at ~26 kDa (S-CP-MyoI) and ~44 kDa (L-CP-MyoI) (Figure 8A). The conjugation of CPMV to COVID-826 was confirmed by the same banding profile (Figure 8C). There was a significant difference between the coated and uncoated particles revealing a higher conjugation efficiency for both peptides following the COAT procedure. For MyoI, the COAT strategy increased the number of conjugated peptides from 68 (-F127) to 85 (+F127), and for COVID-826, the COAT strategy increased the number of conjugated peptides from 61 (-F127) to 68 (+F127). The analysis of CPMV-MyoI particles indicated ~60% modification of S-CP and ~80% modification of L-CP following the COAT process, compared to ~72% modification of S-CP and ~41% modification of L-CP without F127. Similarly, the analysis of CPMV-826 particles indicated ~62% modification of S-CP and ~50% modification of L-CP following the COAT process, compared to ~54% modification

of S-CP and ~47% modification for L-CP without F127. In the case of MyoI, the COAT strategy therefore appears to shift the multivalent display tendency from S-CP to L-CP while increasing the overall conjugation efficiency, which should be investigated in more detail. The COAT strategy also enhanced the stability of the plant VNP-peptide conjugates. The aggregation of particles lacking the F127 coat was indicated by the presence of CPMV-MyoI(-F127) particles trapped in the wells of agarose gels leading to the colocalization of the CPMV protein and RNA signals (Figure 8B) and the formation of visible pellets by both the CPMV-MyoI(-F127) and CPMV-826(-F127) particles (Figure 8D). Furthermore, SDS-PAGE analysis of the CPMV-MyoI(-F127) particles revealed a band corresponding to the free peptide in lane 2 (Figure 8A), suggesting the free peptide precipitates in the CPMV-MyoI(-F127) pellet and cannot be purified (Figure 8D). In contrast, samples prepared using the COAT process were dispersed and soluble with no signs of aggregation. There were also no signs of aggregation in the TEM images (Figure 8E). DLS confirmed the significant aggregation of the CPMV-MyoI(-F127) and CPMV-826(-F127) particles. The Zaverage of the CPMV-MyoI(-F127) particles was ~913.7 nm (PDI = 0.240), and that of the CPMV-826(-F127)particles was  $\sim 112.6$  nm (PDI = 0.578), compared to  $\sim 39.8$ nm (PDI = 0.138) for the CPMV-MyoI(+F127) particles and  $\sim$ 43.3 nm (PDI = 0.132) for the CPMV-826(+F127) particles (Figure 8F). The CPMV-MyoI(+F127) sample included a small proportion of larger particles that were not detected



Figure 10. Chemical conjugation of peptides COVID-106, COVID-153, COVID-454, and CH401R to CPMV using maleimide-thiol chemistry. (A) SDS-PAGE analysis of CPMV conjugates to SARS-CoV-2 peptides. S-CP = CPMV small coat protein ( $\sim$ 24 kDa) and L-CP = CPMV large coat protein ( $\sim$ 42 kDa). (B) Characterization of CPMV-CH401R particles by SDS-PAGE and agarose gel electrophoresis. (C) Densitometric comparison of conjugates produced using the FORMCOAT strategy and conventional bioconjugation. (D) Photograph of CPMV-peptide particles with/without (+/-) the FORMCOAT preincubation strategy, showing aggregation in the sample without preincubation. (E) Photograph of CPMV-peptide particles prepared with and without the prior formulation of peptides in F127 micelles, showing aggregation for the samples without prior peptide formulation. (F) Corresponding DLS intensities of CPMV-peptide particles ( $Z_{av}$  data are mean values  $\pm$  SD, n=3). (G) Corresponding TEM images of negatively stained CPMV particles.

visually in the solution (Figure 8D) or in the TEM images (Figure 8E).

**2.3. Ligand Formulation (FORMCOAT Strategy).** 2.3.1. General Strategy. The three remaining SARS-CoV-2 epitopes (COVID-106, COVID-153, and COVID-454) as well as the HER2 epitope CH401R required additional F127 preincubation because the peptides were insoluble in the 0.01

M potassium phosphate reaction buffer (pH 7.4). We therefore applied a formulation method adapted from a protocol in which the hydrophobic cyclosporine A peptide (Log P = 2.92) was micellized with F127 following dialysis-driven DMSO-aqueous exchange. F127 was used to package the four hydrophobic peptides into micellized, water-soluble formulations (Figure 9). Accordingly, each peptide was dissolved in

Table 2. Secondary Structure Peptide Ranking by Decreasing log P and Associated Empirical F127 Conditions Required for Stable Plant VNP Bioconjugation a,b

		3D method				
peptide	MW (Da) <sup>b</sup>	log P <sup>a</sup>	log S <sup>a</sup>	isoelectric point (pH) <sup>b</sup>	net charge @ pH 7 <sup>b</sup>	estimated water solubility <sup>b</sup>
ApoAI-4FN	2631	1.53	-5.43	6.36	-0.1	good
CH401-rat	2922	1.19	-5.11	8.54	0.9	poor
myostatin 1	2092	1.06	-5.18	8.96	1.2	poor
COVID-153	2158	0.98	-5.47	9.73	2	poor
COVID-106	2043	0.84	-5.21	9.12	0.9	poor
F3	3707	0.81	-5.18	11.08	7.9	good
COVID-636	1761	0.47	-4.94	7.09	0	poor
COVID-454	2164	0.32	-4.81	8.79	0.9	poor
ScG3	1809	0.27	-5.1	8.96	1	poor
COVID-826	2380	0.27	-4.70	10.08	1.9	good
COVID-1159	1872	0.24	-5.15	7.09	0	good
COVID-386	2261	-0.06	-5.25	9	1.9	poor
COVID-579	2401	-0.10	-4.81	9.06	0.9	good
COVID-469	2124	-0.20	-5.01	10.22	1.9	good
COVID-820	1990	-0.39	-4.15	6.26	-0.1	good
COVID-420	1857	-0.55	-4.38	6.21	-0.1	good
COVID-564	1741	-0.89	-5.03	9.07	0.9	good

COAT FORMCOAT N/A

DMSO and mixed with 10% (w/w) F127 before dialysis to form peptide-loaded micelles that are stable in aqueous buffer. The formulated peptides (FORM) were then combined with CPMV-MPEG<sub>4</sub> particles that had already been coated with F127 (COAT), in what we describe as the FORMCOAT strategy (Scheme 3).

2.3.2. Peptide Conjugation Using the FORMCOAT Strategy. The formulated peptides were mixed with the CPMV-M(PEG)<sub>4</sub> particles coated with F127 at a peptidedependent molar excess, and the reaction mix was purified by low-temperature ultracentrifugation to remove excess peptide and F127. The pellets were washed three times in 0.01 M potassium phosphate buffer (pH 7.4) before characterization using the methods discussed above. In each case, uncoated particles were conjugated to the same peptides as controls. The conjugation of CPMV to peptides CH401R (~2.9 kDa), COVID-106 (~2.0 kDa), COVID-153 (~2.2 kDa), and 481 COVID-454 (~2.2 kDa) was confirmed by SDS-PAGE, which revealed the presence of native CPMV S-CP and L-CP subunits as well as higher-molecular-weight bands representing the same subunits displaying each peptide (Figure 10A,B). Densitometric analysis using ImageJ (Figure 10C) confirmed that the FORMCOAT method enhanced conjugation efficiency by 11-40% compared to the samples lacking F127, thus increasing the number of peptide ligands per plant VNP. Furthermore, conjugates prepared using the FORMCOAT method were stable and soluble, without visible aggregation (Figure 10D,E), whereas control samples lacking F127 showed visible signs of aggregation because of the formation of insoluble conjugates. SDS-PAGE also revealed bands at the bottom of the gel, indicating that the insoluble peptides were not removed by purification (Figure 10A lanes 2 and 4; Figure 10B lane 2). DLS confirmed that the polydispersity of CPMV conjugates prepared using the FORMCOAT strategy was lower (PDI < 0.120) than the corresponding samples lacking an F127 coat (PDI > 0.433), and the intensity peak profile was similar to that of native CPMV (Figure 10F). The Z-average of the FORMCOAT

CPMV-peptide particles ranged from  $\sim$ 34 to  $\sim$ 42 nm, whereas the corresponding values for the particles lacking F127 ranged from  $\sim$ 436 to  $\sim$ 5149 nm. The CPMV-153 FORMCOAT particles displayed some trace aggregates. However, the samples lacking F127 featured irregular peak shapes unsuitable for measurement, probably reflecting the presence of complex, heterogeneous precipitates of plant VNP-peptide conjugates and the free peptide, as indicated by SDS-PAGE analysis. TEM images confirmed the integrity of the CPMV-peptide conjugates generated using the FORMCOAT strategy (Figure 10G).

**2.4.** Retroanalysis of F127-Mediated Bioconjugation and Chemoinformatic Prediction. Ab initio secondary and tertiary structure prediction tools are particularly useful during the early stage of rapid response initiatives to combat emerging biological threats with undefined structural features. Preliminary nucleotide and peptide sequences allow such tools to generate potentially useful 3D information that can be synergized with log P calculators to improve the approximation of peptide ligand hydrophobicity, which predicts the feasibility of chemical fusion and multivalent display on nanoparticles. The virtual prescreening of peptide or ligand candidates prior to bioconjugation can save time and resources.

To demonstrate how ligand hydrophobicity calculations could inform about peptide-plant virus nanoparticle bioconjugation strategies, we retroactively analyzed 17 unique peptide sequences using the PEP-FOLD3 secondary structure prediction tool in concert with ALOGPS v2.1 freeware to predict Log *P* values. PDB output files from PEP-FOLD3 were converted to 3D Sybyl mol2 or linear SMILES format using Open Babel v2.4.0 freeware for corresponding log *P* predictions (Table 2 and Tables S1 and S2 provide a summary of DLS data comparing the FORMCOAT method versus conventional bioconjugation). Accordingly, the peptides were assigned to three categories representing the F127 strategy required for stable conjugation: COAT (blue), FORMCOAT (yellow), and N/A (blank). The N/A category consists of peptides that can be conjugated to CPMV without

<sup>&</sup>lt;sup>a</sup>Calculated using ALOGPS2.1 (log *P* is the octanol/water partition coefficient, with higher values representing increasing lipophilicity). <sup>b</sup>Calculated using PepCalc (the isoelectric point is the pH condition at which the net charge of the peptide is zero).

aggregation using conventional bioconjugation methods. <sup>50</sup> The log *P* values generated using this approach fell within the range of values reported in the literature. <sup>51</sup>

After first ranking the peptides in order of decreasing hydrophobicity (decreasing log P), we then cross-mapped our empirical selection of the FORMCOAT or COAT methods to generate stable CPMV-peptide conjugates and observed a strong correlation. The data suggested that solubility would be challenging for ligands with calculated log P values >0.24, and this could be addressed using the micelle formulation COAT and FORMCOAT strategy (Table 2). It is important to note that the standard in-house molecule/peptide library from ALOGPS 2.1 was used for log P calculations, but the freeware offers users an option to import custom libraries of compounds to better tailor their predictions. Furthermore, secondary structure prediction software can improve the accuracy of log P prediction, as suggested by the tighter correlation observed between log P values and the F127 formulation method when using 3D models (Table 2) rather than linear models (Table S1). This dataset lies at the intersection of chemoinformatics and empirical measurements and demonstrates that, without any prior knowledge other than a peptide sequence, it is possible to predict the secondary structure, use this model as input for the Log P calculation, and from there predict whether the COAT or FORMCOAT strategy is required for successful plant VNP bioconjugation (log P > 0.24). A bioconjugation workflow decision tree incorporating this concept is shown in Figure S7.

## 3. CONCLUSIONS

We have improved the efficiency and stability of plant VNP bioconjugation to 11 hydrophobic ligands, including four that are insoluble without F127 micellar formulation combined with the coating of plant VNPs with F127. Initially, we used F127-coated plant VNP systems as a temporary scaffold to enable multivalent display of hydrophobic ligands, mitigate aggregation, and generate stable solutions containing plant VNP conjugates (COAT strategy). In parallel, we used F127 to formulate and repackage hydrophobic ligands into watersoluble micelles that can be combined with the F127-coated plant VNPs (FORMCOAT strategy). To the best of our knowledge, this is the first time that F127 has been used in this manner to facilitate the bioconjugation of a hydrophobic ligand to a hydrophilic nanocarrier, and more specifically, a plant virus nanoparticle. This overcomes a significant barrier caused by the insolubility of inherently hydrophobic peptides and allows the preparation of pure plant VNP-peptide conjugates without significant aggregation. The improvements in conjugation efficiency and stability will maximize the impact of such conjugates in real-world applications and will be followed up by analyzing their biological activity. For example, a recent COVID-19 study indicates that plant VNP-peptide vaccines generated using F127 methods detailed above are immunogenic in vivo. 50 Finally, the utilization of chemoinformatic genic in vivo.50 prediction software (particularly log P) will accelerate the development of conjugates by circumventing unnecessary screening steps.

## 4. EXPERIMENTAL SECTION

**4.1. Synthesis and Formulation Materials.** Pluronic F127 was purchased from Sigma-Aldrich (St Louis, MO, USA). DMSO was purchased from VWR International (Radnor, PA, USA). Cy5.5 NHS ester was purchased from Lumiprobe (Hunt Valley, MD, USA). Avm

was synthesized in-house (Figure S1). All peptide ligands were prepared by solid-phase peptide synthesis and purchased from GenScript (Piscataway, NJ, USA). SM(PEG)4, boric acid, monobasic dihydrogen phosphate, and dibasic monohydrogen phosphate were purchased from Thermo Fisher Scientific (Waltham, MA, USA). CPMV and TMV-Lys (described throughout this article as TMV for simplicity) were produced in plants as previously described<sup>6,52</sup> and were quantified in plant extracts by UV/Vis spectroscopy (CPMV  $\varepsilon_{260 \text{nm}} = 8.1 \text{ mg}^{-1} \text{ mL cm}^{-1}$ ; TMV  $\varepsilon_{260 \text{nm}} = 3 \text{ mg}^{-1} \text{ mL cm}^{-1}$ ). Virus integrity was determined by TEM (see below). TMGMV was purchased from Bioprodex (Gainesville, FL, USA), purified by ultracentrifugation followed by overnight dialysis at 4 ° C using a Spectrum Labs 10 kDa dialysis membrane (Thermo Fisher Scientific), and finally quantified by UV/vis (TMGMV  $\varepsilon_{260\mathrm{nm}} = 3.16~\mathrm{mg}^{-1}~\mathrm{mL}$ cm<sup>-1</sup>). CPMV stock was stored in 0.1 M potassium phosphate buffer (pH 7.0), whereas TMV and TMGMV stocks were stored in 0.01 M potassium phosphate buffer (pH 7.4).

**4.2. Pluronic F127 Coating of Plant VNPs (COAT Strategy).** Plant VNPs were mixed with 4% (w/w) F127 in a total volume of 0.5–1 mL followed by three temperature cycles of 1 min on ice (vortex 10 s) and 5 min at room temperature (vortex 10 s). For TMV, F127 (28 molar equivalents per CP) was applied to 2 mg of native particles before conjugation to Cy5.5 (Scheme 1A) or to the intermediate particle TMV-M(PEG)<sub>4</sub> before conjugation to peptides (Scheme 1B). For TMGMV, F127 (28 molar equivalents per CP) was applied to 2 mg of the intermediate particle TMGMV-ds before conjugation to Avm. For CPMV, F127 (480 molar equivalents per particle) was applied to 2 mg of the intermediate particle CPMV-M(PEG)<sub>4</sub> before conjugation to peptides.

- **4.3. Pluronic F127 Formulation of Ligands.** Hydrophobic ligands insoluble in water were dissolved in anhydrous DMSO (10 mg/mL) and mixed with 10% (w/w) F127. We then dialyzed 1 mL of the resulting solution against 1 L 0.01 M potassium phosphate buffer (pH 7.4) using a 1 kDa dialysis membrane, stirring for 2 h at room temperature. Fresh buffer was provided after 30 and 60 min. Formulated ligands were then combined with coated plant VNPs (FORMCOAT strategy).
- **4.4.** Bioconjugation of Cy5.5 NHS Ester to TMV Lysine Residues (Native Chemical Ligation). Cy5.5 NHS ester was mixed with native TMV particles (two molar equivalents per CP) already coated with F127 using the COAT strategy, and the reaction was allowed to proceed for 30 min at room (Scheme 1A). The TMV-Cy5.5 particles were purified by low-temperature ultracentrifugation at  $52,000 \times g$  for 1 h on a 30% (w/v) sucrose cushion.
- 4.5. Bioconjugation of Avm to TMGMV Tyrosine Residues (Click-Chemistry). A diazonium salt was prepared by reacting 75  $\mu$ L 3 M sodium nitrite with 25  $\mu$ L 0.68 M 3-ethylaniline in 400  $\mu$ L 0.3 M p-toluenesulfonic acid monohydrate for 1 h on ice. We then added 15 molar equivalents of the diazonium salt to a 2 mg/mL final concentration of TMGMV in 10 mM borate buffer (pH 8.8) for 30 min on ice (Scheme 1B). The TMGMV-ds intermediate was purified by low-temperature ultracentrifugation at 52,000  $\times$  g for 1 h on a 30% w/v sucrose cushion. Particles were resuspended in 0.01 M potassium phosphate buffer (pH 7.4) overnight at 4 °C. We then applied the COAT preincubation strategy prior to Avm conjugation (Scheme 1B) with uncoated particles as controls. Coated and uncoated particles were incubated with the Avm ligand (five molar equivalents per CP), along with 2 mM aminoguanidine, 2 mM L-ascorbic acid sodium salt, and 1 mM copper(II) sulfate in 0.01 M potassium phosphate buffer (pH 7.4) for 0.5, 3, or 24 h on ice. The TMGMV-Avm product was purified by low-temperature ultracentrifugation at 52,000  $\times$  g for 1 h on a 30% w/v sucrose cushion. An indirect fluorescence assay was used to infer the number of Avm ligands conjugated to TMGMV. Briefly, two molar equivalents of sulfo-Cy5.5-azide were reacted with TMGMV-ds and TMGMV-Avm for 30 min on ice in 0.01 potassium phosphate buffer. The difference in Cy5.5 loading between the TMGMV and TMGMV-Avm formulations was taken as the number of Avm ligands conjugated to TMGMV.
- 4.6. Bioconjugation of Peptide Ligands to TMV/CPMV Lysine Residues (Maleimide Chemistry). External lysine residues

were reacted with the SM(PEG)<sub>4</sub> linker at 25 molar equivalents per TMV CP or five molar equivalents per CPMV CP (2 mg/mL final plant VNP concentration in 0.01 M potassium phosphate buffer, pH 7.4) for 2 h at room temperature. Plant VNP-M(PEG)<sub>4</sub> intermediates were purified by low-temperature ultracentrifugation at  $52,000 \times g$  for 1 h on a 30% w/v sucrose cushion. We then applied the COAT procedure, and untreated particles were used as controls. Plant VNP-M(PEG)<sub>4</sub> samples with or without the F127 coating were incubated with hydrophobic peptide ligands, including those formulated with F127 micelles (Scheme 3). For TMV-F3 and TMV-ScG3, the peptide was reacted with TMV-M(PEG)<sub>4</sub> at 0.5 molar equivalents per CP. For CPMV-ApoAI, the peptide was reacted with CPMV-M(PEG)<sub>4</sub> at 200 molar equivalents per particle. For CPMV-MyoI, the SARS-CoV-2 peptides, and for CPMV-CH401R, the peptides were reacted at 3000 molar equivalents per particle. Reactions with TMV and CPMV were carried out at room temperature and lasted for 2 and 12 h, respectively. Conjugates were purified by low-temperature ultracentrifugation at  $52,000 \times g$  for 1 h on a 30% w/v sucrose cushion. Pellets were washed three times in 0.01 M potassium phosphate buffer (pH 7.4) and were resuspended prior to analysis.

- **4.7. UV/vis Spectroscopy.** UV/visible spectra of native and modified CPMV, TMV, and TMGMV nanoparticles were recorded using a NanoDrop spectrophotometer (Thermo Fisher Scientific). Samples were dispersed in 0.01 M potassium phosphate buffer (pH 7.4). The number of Cy5 fluorophores per TMGMV CP was determined based on the ratio and the Beer–Lambert law: TMV-Lys  $\varepsilon$  (260 nm) = 3.0 mL mg<sup>-1</sup> cm<sup>-1</sup>, molecular weight = 39.4 × 10<sup>6</sup> g mol<sup>-1</sup>; CPMV  $\varepsilon$  (260 nm) = 8.1 mL mg<sup>-1</sup> cm<sup>-1</sup>, molecular weight = 6 × 10<sup>6</sup> g mol<sup>-1</sup>; TMGMV  $\varepsilon$  (260 nm) = 3 mL·mg<sup>-1</sup> cm<sup>-1</sup>, molecular weight = 39.4 × 10<sup>6</sup> g mol<sup>-1</sup>; Cy5.5  $\varepsilon$  (684 nm) = 198,000 M<sup>-1</sup> cm<sup>-1</sup>, molecular weight = 768 Da.
- **4.8. SDS-PAGE.** We denatured 5  $\mu$ g of plant VNP-peptide conjugates and controls at 100 °C for 5 min in 4× LDS loading dye and 10× reducing solution with a final volume of 20  $\mu$ L. Denatured plant VNP CPs and SeeBlue Plus2 ladder were loaded onto 4–12% or 12% NuPAGE precast gels in 1× 3-(N-morpholino)propanesulfonic acid buffer. The samples were separated for 37 min at 200 V and 120 mA. Gels were photographed using the FluorChem R imaging system under white light for Coomassie Brilliant Blue detection and MultiFluor Red light for Cy5.5 detection.
- **4.9. Agarose Gel Electrophoresis.** We loaded 10  $\mu$ g of CPMV-peptide conjugates and controls onto a 1.2% (w/v) TAE agarose gel and separated the samples at 120 V for 30 min. Gels were photographed using the FluorChem R imaging system.
- **4.10. DLS.** The hydrodynamic diameter of native and conjugated plant VNPs was determined by diluting the samples to 1 mg/mL in 0.01 M potassium phosphate buffer (pH 7.4) followed by measurement using a Zetasizer Nano ZSP/Zen5600 instrument (Malvern Panalytical, Malvern, UK). The particle length was calculated as the weighted mean of the intensity distribution.
- **4.11. TEM.** TMV samples were diluted to 0.5 mg/mL in Milli-Q water, and CPMV samples were diluted to 0.2 mg/mL for optimal sample deposition. We adsorbed 10  $\mu$ L of each diluted plant VNP sample onto FCF400-CU 400-mesh copper grids (Electron Microscopy Sciences, Hatfield, PA, USA) for 2 min at room temperature, then washed the grid twice for 30 s with Milli-Q water, and stained the sample with 10  $\mu$ L 2% (w/v) uranyl acetate for 1 min. The grid was blotted with Whatman filter paper to remove excess solution and examined at 80 kV using a FEI Company (Hillsboro, OR, USA) Tecnai G2 Spirit transmission electron microscope.
- **4.12. Chemoinformatic Prediction.** For 3D peptide analysis, the highest probability secondary structure model generated by PEP-FOLD3 was downloaded as a PDB file and converted to Sybyl mol2 format using Open Babel v2.4.0. For linear peptide analysis, PDB output files from PEP-FOLD3 were converted to SMILES format also using Open Babel. For linear small-molecule analysis, CDX files from ChemDraw were converted to SMILES format also using Open Babel. All input files were uploaded into ALOGPS v2.1 with the corresponding input formats to retrieve predicted Log *P* and Log *S*

values. Peptides and small molecules were considered in separate tables because of the intrinsic differences in ligand sizes and chemical properties.

#### ASSOCIATED CONTENT

## **Solution** Supporting Information

The Supporting Information is available free of charge at https://pubs.acs.org/doi/10.1021/acsami.1c13183.

The synthesis of Avm and its characterization by ESI-MS and FT-IR spectroscopy (Figures S1 and S2), FT-IR, ELISA, and DLS of F127-treated plant VNPs (Figures S3—S5, Table S2), the quantification of Cy5 conjugated to TMV with and without F127 (Figure S6), peptide properties (Log *P* values, Table S1), and the proposed bioconjugation decision tree (Figure S7) (PDF)

#### AUTHOR INFORMATION

## **Corresponding Author**

Nicole F. Steinmetz – Department of NanoEngineering, Center for Nano-ImmunoEngineering, Institute for Materials Discovery and Design, Department of Bioengineering, Department of Radiology, and Moores Cancer Center, University of California San Diego, La Jolla, California 92039, United States; orcid.org/0000-0002-0130-0481; Email: nsteinmetz@ucsd.edu

#### **Authors**

- Matthew D. Shin Department of NanoEngineering and Center for Nano-ImmunoEngineering, University of California San Diego, La Jolla, California 92039, United States
- Justin D. Hochberg Department of NanoEngineering, University of California San Diego, La Jolla, California 92039, United States
- Jonathan K. Pokorski Department of NanoEngineering, Center for Nano-ImmunoEngineering, and Institute for Materials Discovery and Design, University of California San Diego, La Jolla, California 92039, United States; orcid.org/0000-0001-5869-6942

Complete contact information is available at: https://pubs.acs.org/10.1021/acsami.1c13183

#### Notes

The authors declare the following competing financial interest(s): Drs. Steinmetz and Pokorski are co-founders of and have financial interest in Mosaic ImmunoEngineering Inc. The other authors have no conflict of interest to declare.

## ACKNOWLEDGMENTS

This work was funded in part by the following grants from the NIH (R01-CA202814, R01-HL137674 to N.F.S.), NSF (RAPID CMMI-2027668 and OISE 1844463 to N.F.S. and J.K.P.), and USDA (NIFA-2020-67021-31255 to N.F.S.) and was partially supported by NSF through the UC San Diego Materials Research Science and Engineering Center (UCSD MRSEC), DMR-2011924 (to N.F.S. and J.K.P.). We thank Dr. Paul L. Chariou for helpful discussions regarding the Avm conjugate.

### REFERENCES

(1) Efthimiadou, E. K.; Theodosiou, M.; Toniolo, G.; Abu-Thabit, N. Y. 15 - Stimuli-Responsive Biopolymer Nanocarriers for Drug

- Delivery Applications. In *Stimuli Responsive Polymeric Nanocarriers for Drug Delivery Applications, Volume 1*; Makhlouf, A. S. H.; Abu-Thabit, N. Y., Eds.; Woodhead Publishing Series in Biomaterials; Woodhead Publishing, 2018; 405–432.
- (2) Herrera Estrada, L. P.; Champion, J. A. Protein Nanoparticles for Therapeutic Protein Delivery. *Biomater. Sci.* **2015**, *3*, 787–799.
- (3) Chariou, P. L.; Ortega-Rivera, O. A.; Steinmetz, N. F. Nanocarriers for the Delivery of Medical, Veterinary, and Agricultural Active Ingredients. *ACS Nano* **2020**, *14*, 2678–2701.
- (4) Veneziano, R.; Moyer, T. J.; Stone, M. B.; Wamhoff, E.-C.; Read, B. J.; Mukherjee, S.; Shepherd, T. R.; Das, J.; Schief, W. R.; Irvine, D. J.; Bathe, M. Role of Nanoscale Antigen Organization on B-Cell Activation Probed Using DNA Origami. *Nat. Nanotechnol.* **2020**, *15*, 716–723.
- (5) Ma, Y.; Nolte, R. J. M.; Cornelissen, J. J. L. M. Virus-Based Nanocarriers for Drug Delivery. *Adv. Drug Deliv. Rev.* **2012**, *64*, 811–825.
- (6) Geiger, F. C.; Eber, F. J.; Eiben, S.; Mueller, A.; Jeske, H.; Spatz, J. P.; Wege, C. TMV Nanorods with Programmed Longitudinal Domains of Differently Addressable Coat Proteins. *Nanoscale* **2013**, *5*, 3808–3816.
- (7) Chariou, P. L.; Steinmetz, N. F. Delivery of Pesticides to Plant Parasitic Nematodes Using Tobacco Mild Green Mosaic Virus as a Nanocarrier. *ACS Nano* **2017**, *11*, 4719–4730.
- (8) Lin, T.; Chen, Z.; Usha, R.; Stauffacher, C. V.; Dai, J.-B.; Schmidt, T.; Johnson, J. E. The Refined Crystal Structure of Cowpea Mosaic Virus at 2.8 Å Resolution. *Virology* **1999**, *265*, 20–34.
- (9) Hesketh, E. L.; Meshcheriakova, Y.; Thompson, R. F.; Lomonossoff, G. P.; Ranson, N. A. The Structures of a Naturally Empty Cowpea Mosaic Virus Particle and Its Genome-Containing Counterpart by Cryo-Electron Microscopy. *Sci. Rep.* **2017**, *7*, 539.
- (10) Schlick, T. L.; Ding, Z.; Kovacs, E. W.; Francis, M. B. Dual-Surface Modification of the Tobacco Mosaic Virus. *J. Am. Chem. Soc.* **2005**, 127, 3718–3723.
- (11) Wang, Q.; Kaltgrad, E.; Lin, T.; Johnson, J. E.; Finn, M. G. Natural Supramolecular Building Blocks: Wild-Type Cowpea Mosaic Virus. *Chem. Biol.* **2002**, *9*, 805–811.
- (12) Abrahamian, P.; Hammond, R. W.; Hammond, J. Plant Virus—Derived Vectors: Applications in Agricultural and Medical Biotechnology. *Annu. Rev. Virol.* **2020**, *7*, 513–535.
- (13) Bamogo, P. K. A.; Brugidou, C.; Sérémé, D.; Tiendrébéogo, F.; Djigma, F. W.; Simpore, J.; Lacombe, S. Virus-Based Pharmaceutical Production in Plants: An Opportunity to Reduce Health Problems in Africa. *Virol. J.* **2019**, *16*, 167.
- (14) Chung, Y. H.; Cai, H.; Steinmetz, N. F. Viral Nanoparticles for Drug Delivery, Imaging, Immunotherapy, and Theranostic Applications. *Adv. Drug Deliv. Rev.* **2020**, *156*, 214–235.
- (15) Wen, A. M.; Steinmetz, N. F. Design of Virus-Based Nanomaterials for Medicine, Biotechnology, and Energy. *Chem. Soc. Rev.* **2016**, *45*, 4074–4126.
- (16) Zierden, H. C.; Ortiz, J. I.; DeLong, K.; Yu, J.; Li, G.; Dimitrion, P.; Bensouda, S.; Laney, V.; Bailey, A.; Anders, N. M.; Scardina, M.; Mahendroo, M.; Mesiano, S.; Burd, I.; Wagner, G.; Hanes, J.; Ensign, L. M. Enhanced Drug Delivery to the Reproductive Tract Using Nanomedicine Reveals Therapeutic Options for Prevention of Preterm Birth. *Sci. Transl. Med.* **2021**, *13* (), DOI: 10.1126/scitranslmed.abc6245.
- (17) Ensign, L. M.; Tang, B. C.; Wang, Y.-Y.; Tse, T. A.; Hoen, T.; Cone, R.; Hanes, J. Mucus-Penetrating Nanoparticles for Vaginal Drug Delivery Protect Against Herpes Simplex Virus. *Sci. Transl. Med.* **2012**, *4*, 138ra79–138ra79.
- (18) Kim, Y. C.; Shin, M. D.; Hackett, S. F.; Hsueh, H. T.; Lima e Silva, R.; Date, A.; Han, H.; Kim, B.-J.; Xiao, A.; Kim, Y.; Ogunnaike, L.; Anders, N. M.; Hemingway, A.; He, P.; Jun, A. S.; McDonnell, P. J.; Eberhart, C.; Pitha, I.; Zack, D. J.; Campochiaro, P. A.; Hanes, J.; Ensign, L. M. Gelling Hypotonic Polymer Solution for Extended Topical Drug Delivery to the Eye. *Nat. Biomed. Eng.* **2020**, *4*, 1053–1062.

- (19) Schopf, L. R.; Popov, A. M.; Enlow, E. M.; Bourassa, J. L.; Ong, W. Z.; Nowak, P.; Chen, H. Topical Ocular Drug Delivery to the Back of the Eye by Mucus-Penetrating Particles. *Transl. Vis. Sci. Technol.* **2015**, *4*, 11–11.
- (20) Yang, M.; Lai, S. K.; Wang, Y.-Y.; Zhong, W.; Happe, C.; Zhang, M.; Fu, J.; Hanes, J. Biodegradable Nanoparticles Composed Entirely of Safe Materials That Rapidly Penetrate Human Mucus. *Angew. Chem. Int. Ed. Engl.* **2011**, *50*, 2597–2600.
- (21) Schneider, C. S.; Xu, Q.; Boylan, N. J.; Chisholm, J.; Tang, B. C.; Schuster, B. S.; Henning, A.; Ensign, L. M.; Lee, E.; Adstamongkonkul, P.; Simons, B. W.; Wang, S.-Y. S.; Gong, X.; Yu, T.; Boyle, M. P.; Suk, J. S.; Hanes, J. Nanoparticles That Do Not Adhere to Mucus Provide Uniform and Long-Lasting Drug Delivery to Airways Following Inhalation. *Sci. Adv.* 2017, 3, No. e1601556.
- (22) Bodratti, A. M.; Alexandridis, P. Formulation of Poloxamers for Drug Delivery. *J. Funct. Biomater.* **2018**, 9 (), DOI: 10.3390/jfb9010011.
- (23) Basak, R.; Bandyopadhyay, R. Encapsulation of Hydrophobic Drugs in Pluronic F127 Micelles: Effects of Drug Hydrophobicity, Solution Temperature, and PH. *Langmuir* **2013**, 29, 4350–4356.
- (24) Liu, Z.; Gu, J.; Wu, M.; Jiang, S.; Wu, D.; Wang, Q.; Niu, Z.; Huang, Y. Nonionic Block Copolymers Assemble on the Surface of Protein Bionanoparticle. *Langmuir* **2012**, *28*, 11957–11961.
- (25) Surface Layer Modification of Poly (d,l-lactic-co-glycolic acid) Nanoparticles with Targeting Peptide: A Convenient Synthetic Route for Pluronic F127—Tuftsin Conjugate | Bioconjugate Chemistry https://pubs.acs.org/doi/10.1021/acs.bioconjchem.8b00156 (accessed 2021-09-28).
- (26) Polymers|Free Full-Text|Pluronic F127-Folate Coated Super Paramagenic Iron Oxide Nanoparticles as Contrast Agent for Cancer Diagnosis in Magnetic Resonance Imaging https://www.mdpi.com/2073-4360/11/4/743 (accessed 2021-09-28).
- (27) Nguyen, K. T.; Vinh Le, D.; Ho Do, D.; Huan Le, Q. Development of Chitosan Graft Pluronic ® F127 Copolymer Nanoparticles Containing DNA Aptamer for Paclitaxel Delivery to Treat Breast Cancer Cells. *Adv. Nat. Sci: Nanosci. Nanotechnol.* **2016**, 7, No. 025018.
- (28) Wen, A. M.; Infusino, M.; De Luca, A.; Kernan, D. L.; Czapar, A. E.; Strangi, G.; Steinmetz, N. F. Interface of Physics and Biology: Engineering Virus-Based Nanoparticles for Biophotonics. *Bioconjugate Chem.* **2015**, *26*, 51–62.
- (29) Bruckman, M. A.; Czapar, A. E.; VanMeter, A.; Randolph, L. N.; Steinmetz, N. F. Tobacco Mosaic Virus-Based Protein Nanoparticles and Nanorods for Chemotherapy Delivery Targeting Breast Cancer. *J. Controlled Release* **2016**, 231, 103–113.
- (30) Chariou, P. L.; Dogan, A. B.; Welsh, A. G.; Saidel, G. M.; Baskaran, H.; Steinmetz, N. F. Soil Mobility of Synthetic and Virus-Based Model Nanopesticides. *Nat. Nanotechnol.* **2019**, *14*, 712–718.
- (31) Cai, H.; Shukla, S.; Wang, C.; Masarapu, H.; Steinmetz, N. F. Heterologous Prime-Boost Enhances the Antitumor Immune Response Elicited by Plant-Virus-Based Cancer Vaccine. *J. Am. Chem. Soc.* **2019**, *141*, 6509–6518.
- (32) Full article: Effects of maternal immunisation against myostatin on post-natal growth and skeletal muscle mass of offspring in mice https://www.tandfonline.com/doi/full/10.1080/09540100801956596 (accessed 2021-05-22).
- (33) Takayama, K.; Noguchi, Y.; Aoki, S.; Takayama, S.; Yoshida, M.; Asari, T.; Yakushiji, F.; Nishimatsu, S.; Ohsawa, Y.; Itoh, F.; Negishi, Y.; Sunada, Y.; Hayashi, Y. Identification of the Minimum Peptide from Mouse Myostatin Prodomain for Human Myostatin Inhibition. *J. Med. Chem.* **2015**, *58*, 1544–1549.
- (34) Lei, C.; Qian, K.; Li, T.; Zhang, S.; Fu, W.; Ding, M.; Hu, S. Neutralization of SARS-CoV-2 Spike Pseudotyped Virus by Recombinant ACE2-Ig. *Nat. Commun.* **2020**, *11*, 2070.
- (35) Poh, C. M.; Carissimo, G.; Wang, B.; Amrun, S. N.; Lee, C. Y.-P.; Chee, R. S.-L.; Fong, S.-W.; Yeo, N. K.-W.; Lee, W.-H.; Torres-Ruesta, A.; Leo, Y.-S.; Chen, M. I.-C.; Tan, S.-Y.; Chai, L. Y. A.; Kalimuddin, S.; Kheng, S. S. G.; Thien, S.-Y.; Young, B. E.; Lye, D. C.; Hanson, B. J.; Wang, C.-I.; Renia, L.; Ng, L. F. P. Two Linear

- Epitopes on the SARS-CoV-2 Spike Protein That Elicit Neutralising Antibodies in COVID-19 Patients. *Nat. Commun.* **2020**, *11*, 2806.
- (36) Wang, H.; Wu, X.; Zhang, X.; Hou, X.; Liang, T.; Wang, D.; Teng, F.; Dai, J.; Duan, H.; Guo, S.; Li, Y.; Yu, X. SARS-CoV-2 Proteome Microarray for Mapping COVID-19 Antibody Interactions at Amino Acid Resolution. ACS Cent. Sci. 2020, 6, 2238–2249.
- (37) Li, Y.; Lai, D.; Zhang, H.; Jiang, H.; Tian, X.; Ma, M.; Qi, H.; Meng, Q.; Guo, S.; Wu, Y.; Wang, W.; Yang, X.; Shi, D.; Dai, J.; Ying, T.; Zhou, J.; Tao, S. Linear Epitopes of SARS-CoV-2 Spike Protein Elicit Neutralizing Antibodies in COVID-19 Patients. *Cell. Mol. Immunol.* **2020**, *17*, 1095–1097.
- (38) Lu, S.; Xie, X.; Zhao, L.; Wang, B.; Zhu, J.; Yang, T.; Yang, G.; Ji, M.; Lv, C.; Xue, J.; Dai, E.; Fu, X.; Liu, D.; Zhang, L.; Hou, S.; Yu, X.; Wang, Y.; Gao, H.; Shi, X.; Ke, C.; Ke, B.; Jiang, C.; Liu, R. The Immunodominant and Neutralization Linear Epitopes for SARS-CoV-2. Cell Rep. 2021, 34, No. 108666.
- (39) Chariou, P. L.; Wang, L.; Desai, C.; Park, J.; Robbins, L. K.; Recum, H. A.; Ghiladi, R. A.; Steinmetz, N. F. Let There Be Light: Targeted Photodynamic Therapy Using High Aspect Ratio Plant Viral Nanoparticles. *Macromol. Biosci.* **2019**, *19*, No. 1800407.
- (40) Park, J.; Gao, H.; Wang, Y.; Hu, H.; Simon, D. I.; Steinmetz, N. F. S100A9-Targeted Tobacco Mosaic Virus Nanoparticles Exhibit High Specificity toward Atherosclerotic Lesions in Apo E-/- Mice. *J. Mater. Chem. B* **2019**, *7*, 1842–1846.
- (41) Sherman, C. B.; Peterson, S. J.; Frishman, W. H. Apolipoprotein A-I Mimetic Peptides: A Potential New Therapy for the Prevention of Atherosclerosis. *Cardiol. Rev.* **2010**, *18*, 141–147.
- (42) Singla, P.; Singh, O.; Sharma, S.; Betlem, K.; Aswal, V. K.; Peeters, M.; Mahajan, R. K. Temperature-Dependent Solubilization of the Hydrophobic Antiepileptic Drug Lamotrigine in Different Pluronic Micelles—A Spectroscopic, Heat Transfer Method, Small-Angle Neutron Scattering, Dynamic Light Scattering, and in Vitro Release Study. ACS Omega 2019, 4, 11251–11262.
- (43) Alexandridis, P.; Holzwarth, J. F.; Hatton, T. A. Micellization of Poly (Ethylene Oxide)-Poly (Propylene Oxide)-Poly (Ethylene Oxide) Triblock Copolymers in Aqueous Solutions: Thermodynamics of Copolymer Association. *Macromolecules* **1994**, 27, 2414–2425.
- (44) Zhang, Y.; Song, W.; Geng, J.; Chitgupi, U.; Unsal, H.; Federizon, J.; Rzayev, J.; Sukumaran, D. K.; Alexandridis, P.; Lovell, J. F. Therapeutic Surfactant-Stripped Frozen Micelles. *Nat. Commun.* **2016**, *7*, 11649.
- (45) Sokolsky-Papkov, M.; Kabanov, A. Synthesis of Well-Defined Gold Nanoparticles Using Pluronic: The Role of Radicals and Surfactants in Nanoparticles Formation. *Polymer* **2019**, *11*, 1553.
- (46) Shin, M. D.; Shukla, S.; Chung, Y. H.; Beiss, V.; Chan, S. K.; Ortega-Rivera, O. A.; Wirth, D. M.; Chen, A.; Sack, M.; Pokorski, J. K.; Steinmetz, N. F. COVID-19 Vaccine Development and a Potential Nanomaterial Path Forward. *Nat. Nanotechnol.* **2020**, *15*, 646–655.
- (47) Lamiable, A.; Thévenet, P.; Rey, J.; Vavrusa, M.; Derreumaux, P.; Tufféry, P. PEP-FOLD3: Faster de Novo Structure Prediction for Linear Peptides in Solution and in Complex. *Nucleic Acids Res.* **2016**, 44, W449–W454.
- (48) Tetko, I. V.; Gasteiger, J.; Todeschini, R.; Mauri, A.; Livingstone, D.; Ertl, P.; Palyulin, V. A.; Radchenko, E. V.; Zefirov, N. S.; Makarenko, A. S.; Tanchuk, V. Y.; Prokopenko, V. V. Virtual Computational Chemistry Laboratory—Design and Description. *J. Comput.-Aided Mol. Des.* **2005**, *19*, 453—463.
- (49) O'Boyle, N. M.; Banck, M.; James, C. A.; Morley, C.; Vandermeersch, T.; Hutchison, G. R. Open Babel: An Open Chemical Toolbox. *Aust. J. Chem.* **2011**, *3*, 33.
- (50) Ortega-Rivera, O. A.; Shin, M. D.; Chen, A.; Beiss, V.; Moreno-Gonzalez, M. A.; Lopez-Ramirez, M. A.; Reynoso, M.; Wang, H.; Hurst, B. L.; Wang, J.; Pokorski, J. K.; Steinmetz, N. F. Trivalent Subunit Vaccine Candidates for COVID-19 and Their Delivery Devices. J. Am. Chem. Soc. 2021, 143, 14748–14765.
- (51) Thompson, S. J.; Hattotuwagama, C. K.; Holliday, J. D.; Flower, D. R. On the Hydrophobicity of Peptides: Comparing Empirical Predictions of Peptide Log P Values. *Bioinformation* **2006**, *1*, 237–241.

(52) Wen, A. M.; Shukla, S.; Saxena, P.; Aljabali, A. A. A.; Yildiz, I.; Dey, S.; Mealy, J. E.; Yang, A. C.; Evans, D. J.; Lomonossoff, G. P.; Steinmetz, N. F. Interior Engineering of a Viral Nanoparticle and Its Tumor Homing Properties. *Biomacromolecules* **2012**, *13*, 3990–4001.